



Contents lists available at ScienceDirect

# Journal of the Mechanical Behavior of Biomedical Materials

journal homepage: [www.elsevier.com/locate/jmbbm](http://www.elsevier.com/locate/jmbbm)

## Engineering the next-generation tin containing $\beta$ titanium alloys with high strength and low modulus for orthopedic applications

Sumit Bahl, Suvam Das, Satyam Suwas, Kaushik Chatterjee\*

Department of Materials Engineering Indian Institute of Science, Bangalore 560012, India

### ARTICLE INFO

#### Keywords:

Ti-Nb-Sn  
Biomedical alloys  
Aging  
Mechanical properties  
Corrosion  
Biocompatibility

### ABSTRACT

Metastable  $\beta$  Ti alloys are the new emerging class of biomaterial for load bearing orthopedic applications. However, these alloys in the single  $\beta$  phase microstructure have insufficient strength for use in load bearing applications. It is imperative to strengthen these alloys by carefully designed thermo-mechanical processing routes that typically involve aging treatment. In this investigation two newly designed Sn based  $\beta$  Ti alloys of composition Ti-32Nb-(2, 4) Sn are evaluated. The effects of Sn content on the mechanical properties and biological performance of these alloys processed through designed thermo-mechanical processing route are investigated. The increase in the Sn content led to a reduction in the elastic modulus of the alloy. An increase in the Sn content increased the aspect ratio of the  $\alpha$  precipitates, which led to a significant strengthening in the alloy while keeping the elastic modulus low. In addition, the corrosion behavior of the alloy was evaluated in simulated body fluid. The Sn containing  $\beta$  alloys have an excellent corrosion resistance as desired for an implant material. The corrosion resistance improved with an increase in Sn content. These alloys were also observed to have excellent cytocompatibility as they not only supported the attachment and proliferation of human mesenchymal stem cells but also their osteogenic differentiation *in vitro*. The combination of high strength, low elastic modulus, superior corrosion resistance and biocompatibility underscores the promise of Sn containing  $\beta$  Ti alloys for use in orthopedic applications.

### 1. Introduction

Metallic implants are extensively used worldwide to treat a spectrum of orthopedic related disorders. Some of the most critical cases include those of dysfunctional knee and hip joints. A new class of metastable  $\beta$  Ti alloys is considered as promising candidates for the next-generation materials for orthopedic implants. The several advantages offered by  $\beta$  Ti alloys include the use of non-toxic alloying elements such as Nb, Mo, Ta, Zr and Sn for the preparation of the alloy; a close match of the elastic moduli of the alloys and human bone; excellent corrosion resistance and high specific strength (Bahl et al., 2016; Bahl et al., 2017a, 2014; Banerjee and Williams, 2013; Gurao et al., 2013; Niinomi et al., 2012; Suresh et al., 2012, 2013). One of the most critical material properties for load bearing orthopedic applications is the high strength. The strength is also important as it governs the fatigue life of a material. The implants are prone to failure by fatigue due to the cyclic nature of loading during use in the human body (Bahl et al., 2015, 2017b; Menciè et al., 2014; Norman et al., 2014; Yoshitani et al., 2016). The strength in the single phase metastable  $\beta$  Ti alloys is lower compared to Ti-6Al-4V alloy, which is currently a popular choice for

load bearing implants due to its high strength. Therefore, significant attention must be drawn towards the strengthening of  $\beta$  Ti alloys for ensuring their successful application as implants. The most widely employed strengthening mechanism in metastable  $\beta$  Ti alloys is the aging treatment that leads to the precipitation of the  $\alpha$  phase. There are several reports on precipitation strengthening of biomedical grade  $\beta$  Ti alloys (Cardoso et al., 2014; Hao et al., 2007; Li et al., 2011; Mohammed et al., 2015). The strengthening by  $\alpha$  precipitation will depend on the composition of the alloy and the design of the thermo-mechanical processing route. The role of the alloy composition and its response to the processing schedule, which incorporates the aging treatment has been largely underutilized for medical grade  $\beta$  Ti alloys and needs continued investigation.

Ti-Nb-Sn (TNS) has emerged as an important group of  $\beta$  Ti alloys with significant potential for application in orthopedics (Griza et al., 2014; Hanada et al., 2005; Hsu et al., 2013; Matsumoto et al., 2007; Miura et al., 2011). The addition of Sn is important to obtain low elastic modulus by suppressing the  $\omega$  phase. In addition, Sn is a strong solid solution strengthener, which contributes to the strengthening of these alloys (Zhang et al., 2013). The Sn content in the alloy is reported to

\* Corresponding author.

E-mail address: [kchatterjee@materials.iisc.ernet.in](mailto:kchatterjee@materials.iisc.ernet.in) (K. Chatterjee).

significantly alter the strength and elastic modulus in TNS alloys by controlling the phase transformations (Griza et al., 2014; Hanada et al., 2005; Hao et al., 2006; Hsu et al., 2013; Matsumoto et al., 2005; Moraes et al., 2014; Wang et al., 2013). The Sn content also affects the corrosion behavior of TNS alloys (Dalmau et al., 2015; Moraes et al., 2014; Rosalbino et al., 2012; Wang et al., 2013; Zheng et al., 2006). However, most of the investigations on the effect of Sn on the properties of TNS alloys were restricted to the solution treated/quenched or cast microstructure. These microstructures can be expected to have insufficient mechanical properties for use in load bearing orthopedic applications. The influence of Sn content on the properties of thermo-mechanically processed TNS alloys with aged microstructures has been not studied extensively.

We recently reported on the precipitation behavior and its effect on the mechanical properties, electrochemical behavior and biocompatibility in an alloy of composition Ti-32Nb-2Sn (wt%) (Bahl et al., 2017a). The addition of 2 wt% Sn suppressed the  $\omega$  phase formation thereby substantially reducing the elastic modulus of the alloy. It was also shown that the control of nanoscale precipitation by heat treatment significantly improved the mechanical properties of the alloy. Sn was found to be an advantageous alloying element to obtain the optimum combination of biomaterial properties. However, the effect of higher Sn content on the precipitation behavior and its effect on the mechanical properties, electrochemical behavior and biocompatibility are as yet unexplored. In this work, another composition with higher Sn content (Ti-32Nb-4Sn) was chosen and compared against Ti-32Nb-2Sn. The aim of this work was to examine the effect of Sn content on aging behavior, mechanical properties, electrochemical behavior and biocompatibility in TNS alloys.

## 2. Experimental

### 2.1. Materials and processing

Ti-32Nb-2Sn (TNS-2) and Ti-32Nb-4Sn (TNS-4) alloy compositions in wt% were prepared by non-consumable vacuum arc melting with high purity (> 99.9%) elemental constituents, namely, Ti, Nb and Sn. The oxygen content of TNS-2 and TNS-4 alloys was found to be 0.27 wt % and 0.15 wt%, respectively. The solidification microstructure of the cast pan cakes was broken by hot rolling rectangular bars at 950 °C. The hot rolled bars were subsequently solution treated at 950 °C for 0.5 h followed by quenching. The solution treated and quenched bars of the TNS-2 and TNS-4 alloys are hereafter referred to as STQ-2 and STQ-4 respectively where STQ refers to solution treated and quenched. The STQ specimens were aged at 500 °C and 600 °C. The specimens for aging were heated at a slow heating rate of 1 °C/min from room temperature (RT) to final aging temperature (500 °C/600 °C) followed by isothermal heating for 6 h. The specimens were air cooled after the aging treatment was completed. The TNS-2 specimens aged at 500 °C and 600 °C are hereafter referred to as A500-2 and A600-2, respectively. Similarly, TNS-4 specimens aged at 500 °C and 600 °C are hereafter referred to as A500-4 and A600-4, respectively. Some of the specimens were heated at 1 °C/min up to 400 °C followed by isothermal treatment for 2 h. These specimens will be referred to as A400-2 and A400-4 for the TNS-2 and TNS-4 alloys, respectively. This heat treatment was done in order to investigate the intermediate microstructures, which lead to the A500 and A600 microstructures.

### 2.2. Microstructural characterization and X-Ray diffraction

The microstructural characterization was performed using scanning electron microscopy (SEM, Ultra 55 Zeiss) and transmission electron microscopy (TEM, FEI Tecnai F30). Specimens for SEM imaging were prepared using standard metallography techniques. TEM foils were prepared using the twin jet electro polishing technique. The electro polishing was performed at 12 V, -30 °C in 10% perchloric acid

electrolyte prepared in methanol. Compositional analysis of the TEM foils was performed using scanning transmission electron microscope (STEM) based energy dispersive spectroscopy (EDS). The phase identification was performed by X-Ray diffraction (XRD) using Cu-K $\alpha$  radiation (PANalytical, X'pert Pro).

### 2.3. Mechanical characterization

The micro-Vickers hardness tests were performed at 200 gf load and 10 s dwell time (CSM Instruments). The indentation derived elastic modulus was also measured using the standard Oliver-Pharr method. Tensile tests were performed until fracture at a strain rate of  $10^{-3}$  s $^{-1}$  (Instron 5967).

### 2.4. Electrochemical characterization

The electrochemical behavior of the alloys in simulated body fluid (SBF) was analyzed using Tafel extrapolation and impedance spectroscopic techniques. The composition of the SBF prepared has been reported elsewhere (Bahl et al., 2014). The specimens were prepared using standard metallographic techniques with final polishing performed with 0.05  $\mu$ m alumina paste. A standard three electrode electrochemical workstation was used having Pt as a counter electrode and saturated calomel electrode (SCE) as a reference electrode (CHI604E, C.H. Instruments). The open circuit potential (OCP) of the specimens was stabilized for 3 h. The impedance spectra were recorded at the OCP in the frequency range  $10^5$ – $10^{-1}$  Hz with 5 mV amplitude. The Tafel plots were recorded at from -0.6 to + 0.4 V at a scan rate of  $2 \times 10^{-4}$  V/s.

### 2.5. X-Ray photoelectron spectroscopy (XPS)

The passive layer formed on TNS alloys was characterized using XPS. Wide and high resolution XPS spectra of the polished specimens were recorded using Al source, 1.486 eV, Kratos Analytical.

### 2.6. Biological studies

The effect of Sn content on biocompatibility was assessed *in vitro* using primary human mesenchymal stem cells (hMSCs) from a 25-year-old male donor (Lonza). hMSCs were cultured in knock-out Dulbecco's modified Eagle medium (DMEM, Invitrogen) supplemented with 15% MSC-qualified fetal bovine serum (FBS). An antibiotic mixture of 1% penicillin-streptomycin (Sigma) was also added. The specimen with dimensions 7 mm  $\times$  7 mm  $\times$  2 mm were machined by electro-discharge machining and finally polished using 0.05  $\mu$ m alumina paste. The specimens were sterilized by immersing in 70% ethanol and exposure to UV for 30 min. Subsequently, they were placed in a 48 well tissue culture well plate and incubated in 200  $\mu$ l of culture medium 24 h prior to seeding cells. Trypsin-EDTA was used to passage the cells and passage 6 was used for all the studies. 400  $\mu$ l cell suspension containing  $5 \times 10^3$  cells was added to each well.

#### 2.6.1. Cell attachment and proliferation

The hMSC attachment and proliferation was measured at 1 day, 3 days and 5 days after seeding using fluorescence microscopy and DNA quantification. Picogreen assay (Invitrogen) was used to quantify DNA. The cells were lysed by incubating specimens in a 200  $\mu$ l solution of 0.2 mg/ml proteinase K (Sigma) and 0.02% sodium dodecyl sulfate (SDS, Sigma) for 24 h at 37 °C. Subsequently, 100  $\mu$ l of picogreen working solution was added to 100  $\mu$ l lysate. The fluorescence reading was measured with a microplate reader (Biotek) at an excitation wavelength of 485 nm and an emission wavelength of 528 nm. Four replicates were used for each sample.

The cells were fixed by incubating the specimens in 3.7% HCHO for 15 min at 37 °C and subsequently permeabilized with 0.2% Triton X-

100 solution (Sigma). The actin filaments were stained using Alexa Fluor 546 dye at 25  $\mu\text{g}/\text{ml}$  concentration. The nuclei were stained with DAPI solution of 0.2  $\mu\text{g}/\text{ml}$  concentration. The cells were imaged using Olympus IX-71 epi-fluorescence microscope.

### 2.6.2. Osteogenic differentiation

The osteogenic differentiation of hMSCs was assessed by measuring alkaline phosphatase (ALP) activity and mineral deposition after 14 days of seeding. The cells were cultured in the complete medium supplemented with osteoinductive factors (50  $\mu\text{M}$  ascorbic acid, 20 mM  $\beta$ -glycerophosphate and 10 nM dexamethasone). The cells were fixed in 3.7% HCHO solution for 30 min. Subsequently, the cells were stained with 1% Alizarin Red S dye (ARS, Sigma) for 30 min. The dye was removed and specimens were washed several times with water to remove any unbound dye. The dye bound to the mineral deposited on the specimen surface was subsequently solubilized in a solution of 0.5 N HCl and 5% SDS for 30 min at 37  $^{\circ}\text{C}$ . The absorbance of the solution was measured at 405 nm using the microplate reader (Biotek).

P-nitrophenyl phosphate (pNPP, Sigma) was used to measure the ALP activity. The cells were lysed by incubating specimens in a solution of 0.1% Triton-X at 37  $^{\circ}\text{C}$  for 24 h. The collected lysate was passed through a freeze-thaw cycle at  $-20^{\circ}\text{C}$ . 100  $\mu\text{l}$  of the lysate was mixed with 100  $\mu\text{l}$  of the pNPP solution. The absorbance was measured at 405 nm after incubating for 15 min at 37  $^{\circ}\text{C}$ . The ALP activity and the mineral content was normalized to the DNA content measured using the picogreen assay.

## 3. Results and discussion

The material properties that are critical for preparing biomedical implants are: (i) microstructural/phase stability, (ii) mechanical

properties, (iii) electrochemical response in the body environment, and (iv) cytocompatibility. Each of these properties has been evaluated in detail and the results are presented in the following sub-sections.

### 3.1. Microstructural stability in TNS alloys

Fig. 1 shows the SEM micrographs and XRD patterns of STQ-2 and STQ-4 specimens. The high angle peaks with low intensity are magnified and presented in the inset. The doublet in peaks is due to  $\text{K}\alpha_1$  and  $\text{K}\alpha_2$  radiations. It can be seen that a single  $\beta$  phase microstructure is retained after quenching from a temperature above the  $\beta$  transus temperature. Thus, the addition of 2 wt% and higher amount of Sn lead to a complete retention of the  $\beta$  phase upon quenching. Sn is known to suppress the formation of  $\omega$  and  $\alpha''$  phases upon quenching or aging thereby retaining the single  $\beta$  phase in titanium alloys (Hao et al., 2006). In the present case, the formation of  $\omega$  phase was suppressed in both TNS-2 and TNS-4 alloys. Even 2 wt% Sn was found to be sufficient to suppress the  $\omega/\alpha''$  formation.

Fig. 2 shows high-resolution SEM micrographs of the aged specimens of TNS-2 and TNS-4 alloys. Aging at 500  $^{\circ}\text{C}$  and above leads to precipitation of  $\alpha$  phase in both the alloys. The XRD patterns of the aged specimens as shown in Fig. 3 confirm that the precipitates are the  $\alpha$  phase. Table 1 summarizes the volume fraction and dimensions of the precipitates in the aged conditions. The volume fraction of  $\alpha$  precipitates was similar whereas their aspect ratio was higher in the aged TNS-4 alloy compared to the aged TNS-2 alloy.

The TEM micrographs of the intermediately aged specimens, A400-2 and A400-4 specimens are shown in Fig. 4. The volume fraction of precipitates was lower whereas their aspect ratio was higher in TNS-4 compared to TNS-2. The crystallography of the precipitates in A400 samples was not confirmed in the present investigation. However, the

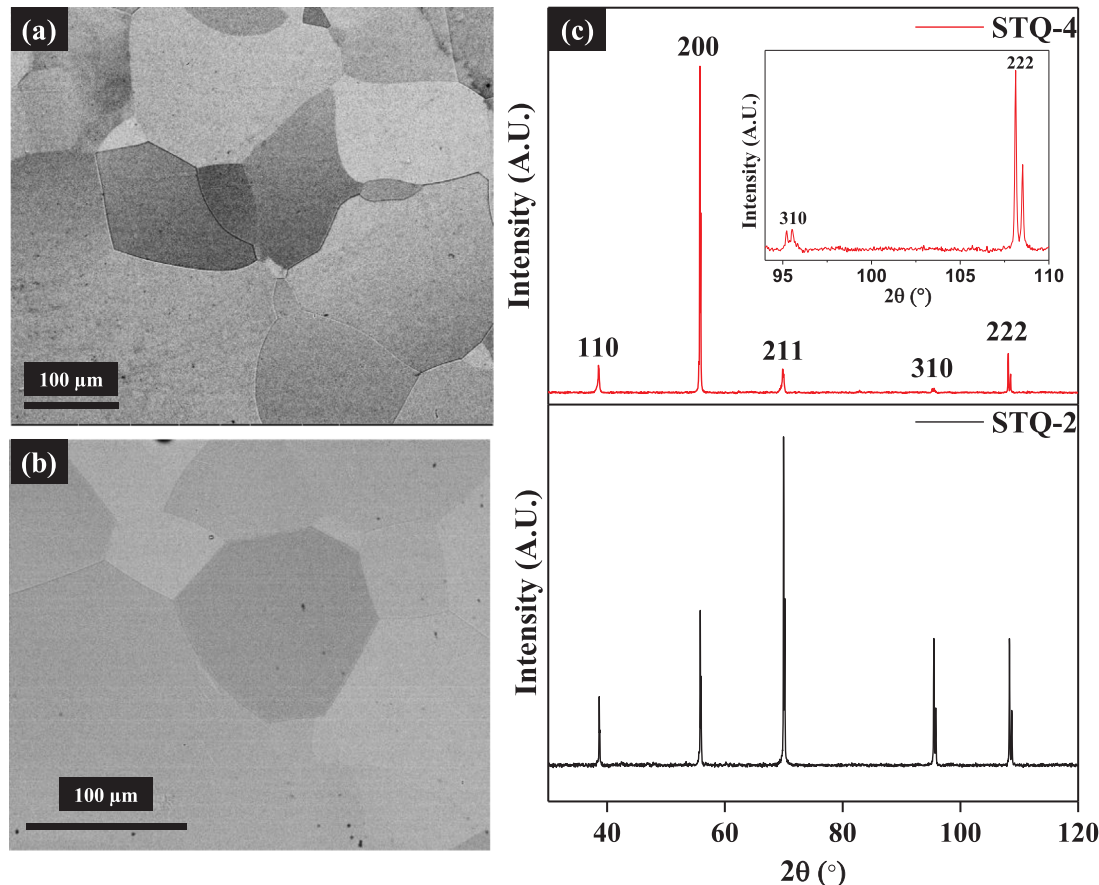


Fig. 1. SEM micrographs of (a) STQ-2 (b) STQ-4 and (c) XRD patterns of STQ-2 and STQ-4 showing the presence of single  $\beta$  phase.

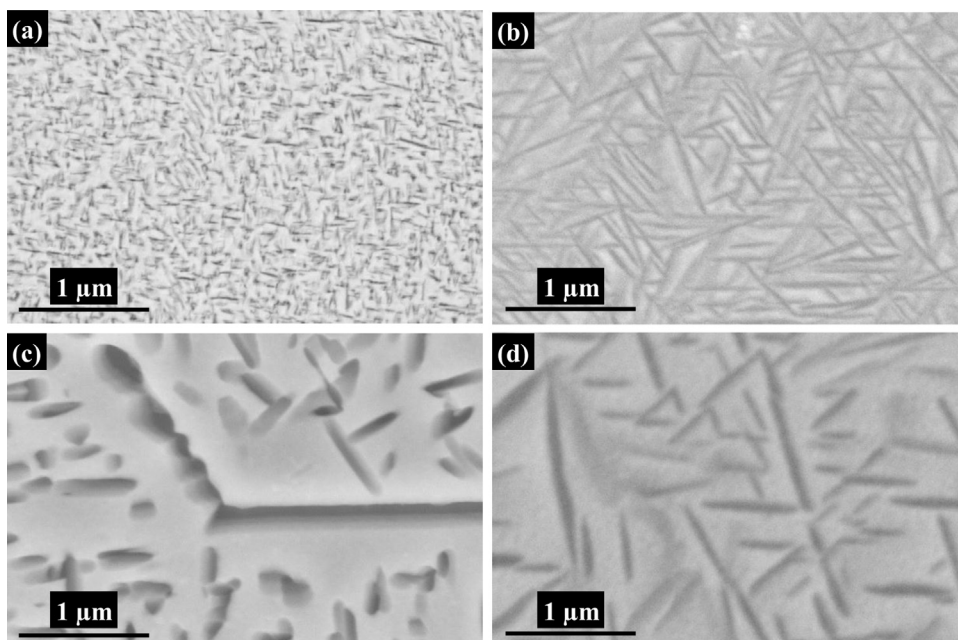


Fig. 2. SEM micrographs of (a) A500-2 (b) A500-4 (c) A600-2 (d) A600-4 showing  $\alpha$  precipitates in the  $\beta$  matrix.

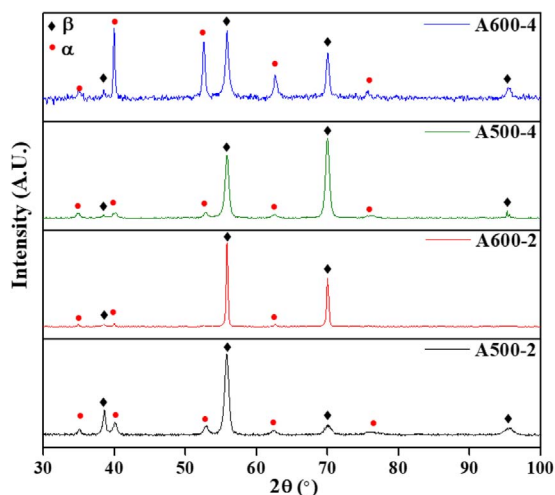


Fig. 3. XRD patterns of the aged specimens showing the presence of  $\alpha + \beta$  phases.

Table 1  
Volume fraction and dimensions of the precipitates in aged microstructures.

Alloy/ Microstructure	Volume fraction %	Length (nm)	Width (nm)	Aspect ratio
A500-2	34	85 ± 20	20 ± 5	4.2
A600-2	23	370 ± 160	130 ± 40	2.8
A500-4	31	330 ± 150	45 ± 10	7.3
A600-4	22	500 ± 300	70 ± 20	7.1

morphology of the precipitates indicates that they could be  $\alpha$  phase. Further characterization will be required to confirm their crystal structure. The elemental partitioning of the alloying elements was characterized using TEM-EDS. The analysis was performed for only A500-4 as a representative condition. The elemental maps of Ti, Nb and Sn are shown in Fig. 5. It can be seen that Ti partitions in the  $\alpha$  phase and Nb partitions in the  $\beta$  phase. The partitioning of Sn is not visually discernible due to the low content of Sn overall in the alloy. However, an intensity profile along the red arrow marked in Fig. 5c as shown in Fig. 5d shows that Sn partitions preferentially in the  $\beta$  phase. Although the partitioning of Sn in the  $\beta$  phase seems weak, it is consistent with

the reported literature wherein Sn was observed to partition preferentially in the  $\beta$  phase of Ti alloys (Bahl et al., 2017a; Salvador et al., 2016; Wang et al., 2017). This suggests that Sn acts as a  $\beta$  stabilizer in Ti-Nb-Sn alloy system.

The size and distribution of the precipitates will depend on the mechanism of nucleation of  $\alpha$  phase in TNS alloys. The TEM micrographs of A400 (Fig. 4) indicate that there are more nucleation sites of  $\alpha$  precipitate in TNS-2 compared to TNS-4. A larger number of nucleation sites leads to a large number precipitates in TNS-2 compared to TNS-4. It is important to note here that the final  $\alpha$  volume fraction is similar in TNS-2 and TNS-4. In such a scenario at equilibrium, a larger number of precipitates in TNS-2 will lead to smaller dimension of the individual precipitates whereas, a smaller number of precipitates in TNS-4 will lead to a larger dimension of the individual precipitates. These results suggest that an increase in the Sn content, which is a  $\beta$  stabilizer, lowers the kinetics of  $\alpha$  precipitation whereas the equilibrium volume fraction of precipitates remains largely unaffected. Consequently, the size and distribution of the precipitates are governed by the kinetics. The plausible effect of lower O content in TNS-4 alloy on lowering the precipitation kinetics, however, cannot be completely discounted. A similar effect of Zr in Ti-Nb-Zr alloys was observed where an increase in the Zr content up to 8 wt% led to a marginal reduction in the volume fraction of  $\alpha$  phase as well as coarsening of the precipitates (Málek et al., 2016). The element Zr behaves similarly to Sn such that it acts as a  $\beta$  stabilizer in the presence of other  $\beta$  stabilizing elements in metastable Ti alloys (Abdel-Hady et al., 2007).

### 3.2. Mechanical properties of TNS alloys

The yield strength is one of the most important mechanical properties of implant materials. As a primary indicator of yield strength, hardness measurements have been performed for each of the alloys for different microstructural conditions. Fig. 6a summarizes the results of the hardness tests. The hardness of STQ-4 (200 HV) is lower compared to STQ-2 (240 HV). Aging at 500 °C increases the hardness in both TNS-2 and TNS-4 alloys. The hardness values are similar (~290 HV) in A500-2 and A500-4 conditions. However, the increase in hardness with respect to the STQ for the same alloy is significantly higher in A500-4 (~90 HV) as compared to A500-2 (50 HV). Aging at 600 °C leads to softening in the TNS-2 alloy. The hardness of A600-2 decreased to 190 HV compared to 240 HV of STQ-2. Aging at 600 °C leads to marginal

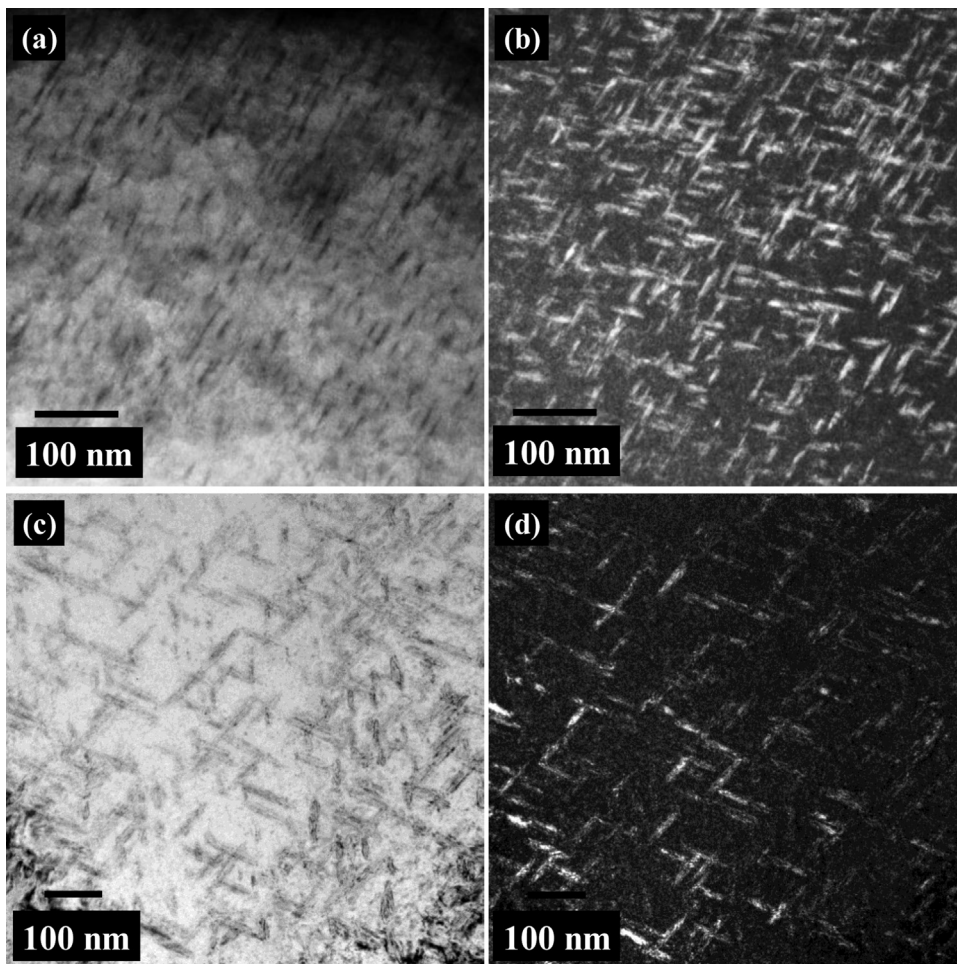


Fig. 4. TEM (a) bright field and (b) dark field micrographs of A400-2; (c) bright field and (d) dark field micrographs of A400-4.

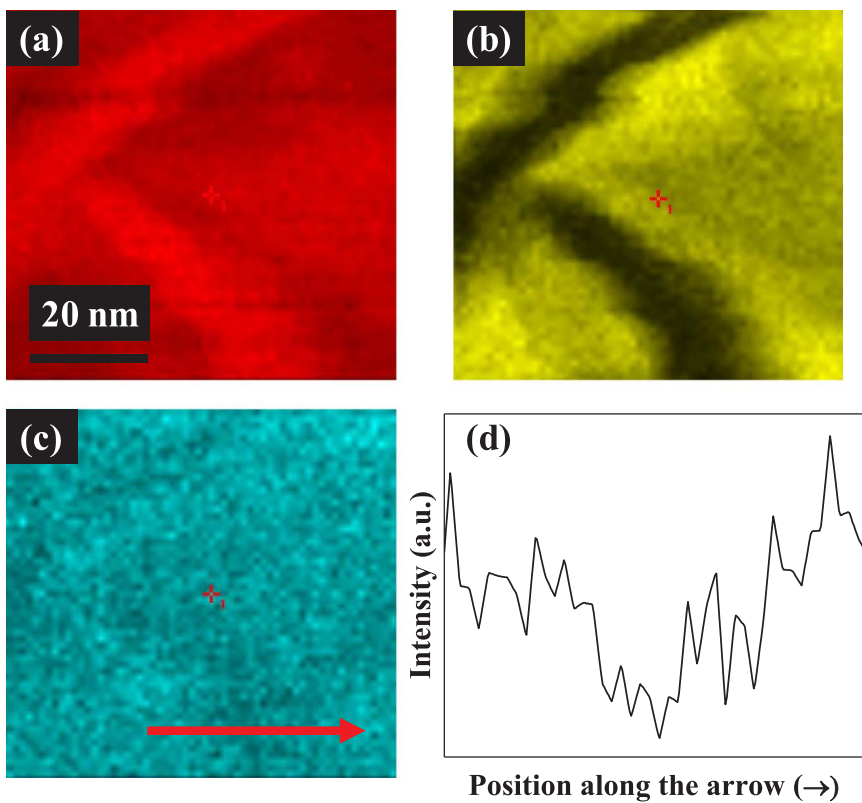


Fig. 5. TEM-EDS elemental maps of (a) Ti, (b) Nb, (c) Sn and (d) line profile showing variation of Sn content along the red arrow marked in (c). (For interpretation of the references to color in this figure legend, the reader is referred to the web version of this article).

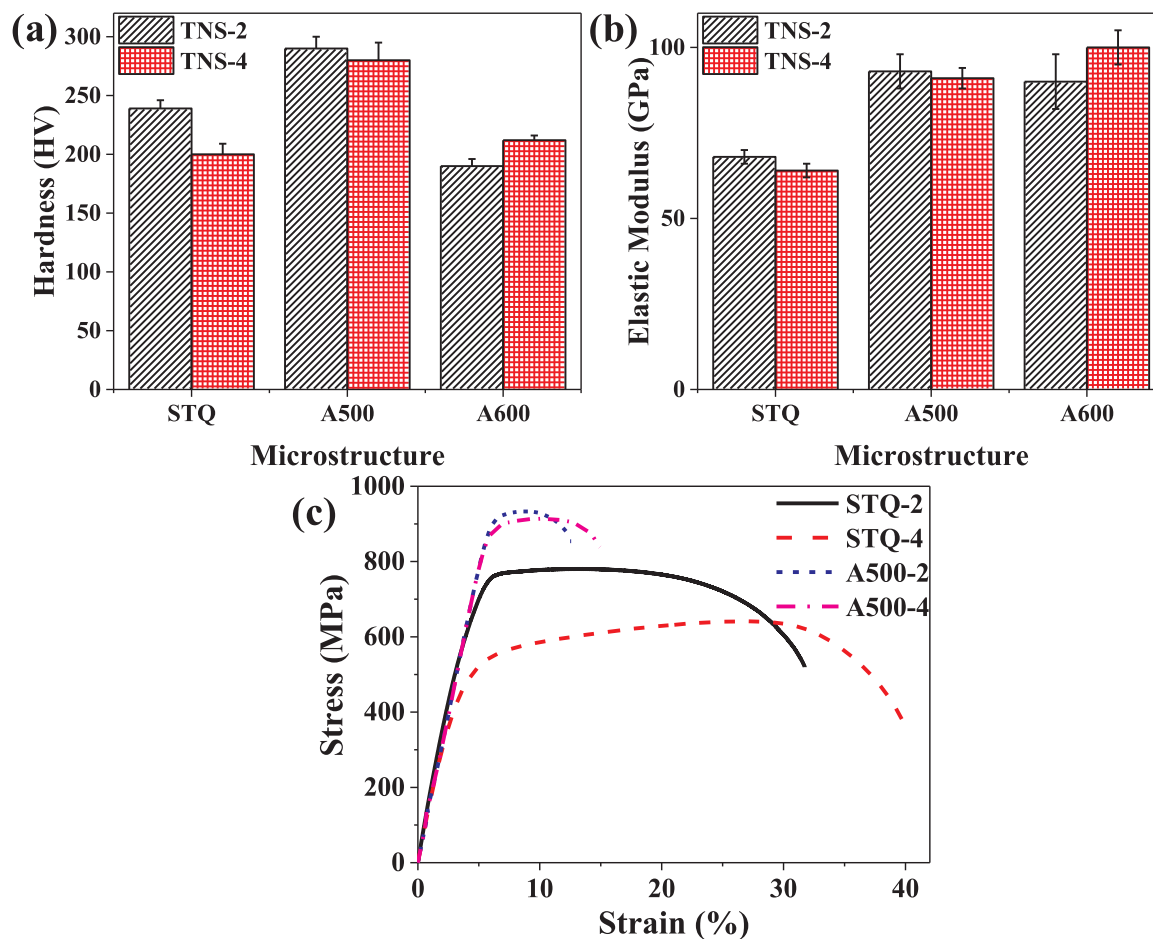


Fig. 6. Plot showing (a) hardness and (b) elastic modulus and (c) tensile stress-strain curves of the TNS-2 and TNS-4 alloys in single phase and dual phase microstructures.

strengthening in TNS-4. The hardness increased from 200 HV in STQ-4 to 210 HV in A600-4. Aside from hardness, yield strength (YS), ultimate tensile strength (UTS) and ductility are important material parameters that were evaluated from tensile tests. The corresponding stress strain curves are shown in Fig. 6c. The tensile tests were not performed for A600 conditions due to limited strengthening, as observed in the hardness tests. The stress-strain data shown in Fig. 6c corroborates the hardness data. The YS and UTS are lower for STQ-4 (YS =  $460 \pm 20$  MPa; UTS =  $640 \pm 15$  MPa) as compared to STQ-2 (YS =  $640 \pm 20$  MPa; UTS =  $760 \pm 30$  MPa). The ductility is higher for STQ-4 ( $42 \pm 4\%$ ) as compared to STQ-2 ( $35 \pm 3\%$ ). The strength increases after aging at 500 °C and is similar for A500-2 (YS =  $870 \pm 15$  MPa; UTS =  $930 \pm 10$  MPa) and A500-4 (YS =  $840 \pm 30$  MPa; UTS =  $900 \pm 30$  MPa). The ductility is also similar for A500-2 ( $12 \pm 1\%$ ) and A500-4 ( $15 \pm 3\%$ ).

The other important mechanical property for the implants is the elastic modulus (E). Fig. 6b shows the indentation based E of the solution treated and aged specimens. The value of E of the STQ-4 (64 GPa) is marginally lower as compared to the STQ-2 (68 GPa). The elastic modulus of the aged specimens of TNS-2 and TNS-4 are similar and in the range of 90–100 GPa.

The lower O content in TNS-4 compared to TNS-2 is likely responsible for the lower hardness of STQ-4 compared to STQ-2. Despite a lower hardness of STQ-4 compared to STQ-2, the hardness is similar in A500-4 and A500-2. Furthermore, hardness is higher for A600-4 compared to A600-2. This implies that the age-hardening effect is more pronounced in TNS-4 compared to TNS-2. Aside from the O content, the strengthening in  $\beta$  Ti alloys is governed by the volume fraction and morphology of the precipitates. Although the O content in TNS-4 alloy was lower compared to TNS-2 alloy, the similar hardness in aged

condition implies that the strengthening is governed by precipitate characteristics rather than by O content. Among the two important precipitate characteristics, the volume fraction was similar whereas, the morphology was different between TNS-2 and TNS-4 alloys. The higher hardening capability of precipitates in TNS-4 can be attributed to the higher aspect ratio of the precipitates. It is reported in the literature that higher aspect ratio of precipitates leads to a higher critical resolved shear stress for the motion of dislocation (Nie, 2003; Nie et al., 1996). The hardness of A600-2 is lower than STQ-2 despite the presence of nanoscale precipitates. This is likely due to the combination of matrix softening and relatively coarser precipitates formed after aging treatment as reported previously (Bahl et al., 2017a). However, softening is not observed in A600-4 likely due to the markedly higher hardening capability of the precipitates in TNS-4. Overall, these results suggest that aging at 500 °C is a viable technique to achieve high strength  $\beta$  Ti alloys desirable for orthopedic applications. The strengthening is also accompanied by an increase in the elastic modulus due to the presence of  $\alpha$  phase, which has modulus higher than  $\beta$  phase. Nevertheless, E is less than 100 GPa which, is significantly lower than E of other Ti alloys such as Ti-6Al-4V ( $\sim 115$  GPa) along with the advantages of comparable strength and presence of non-toxic alloying elements.

Based on the above studies, owing to the most suitable microstructural and mechanical properties of the implant, the further electrochemical and biological characterization was performed only for STQ and A500 conditions in both the alloys. The A600 conditions were not considered further since the strengthening was less compared to A500 conditions with similar elastic modulus.

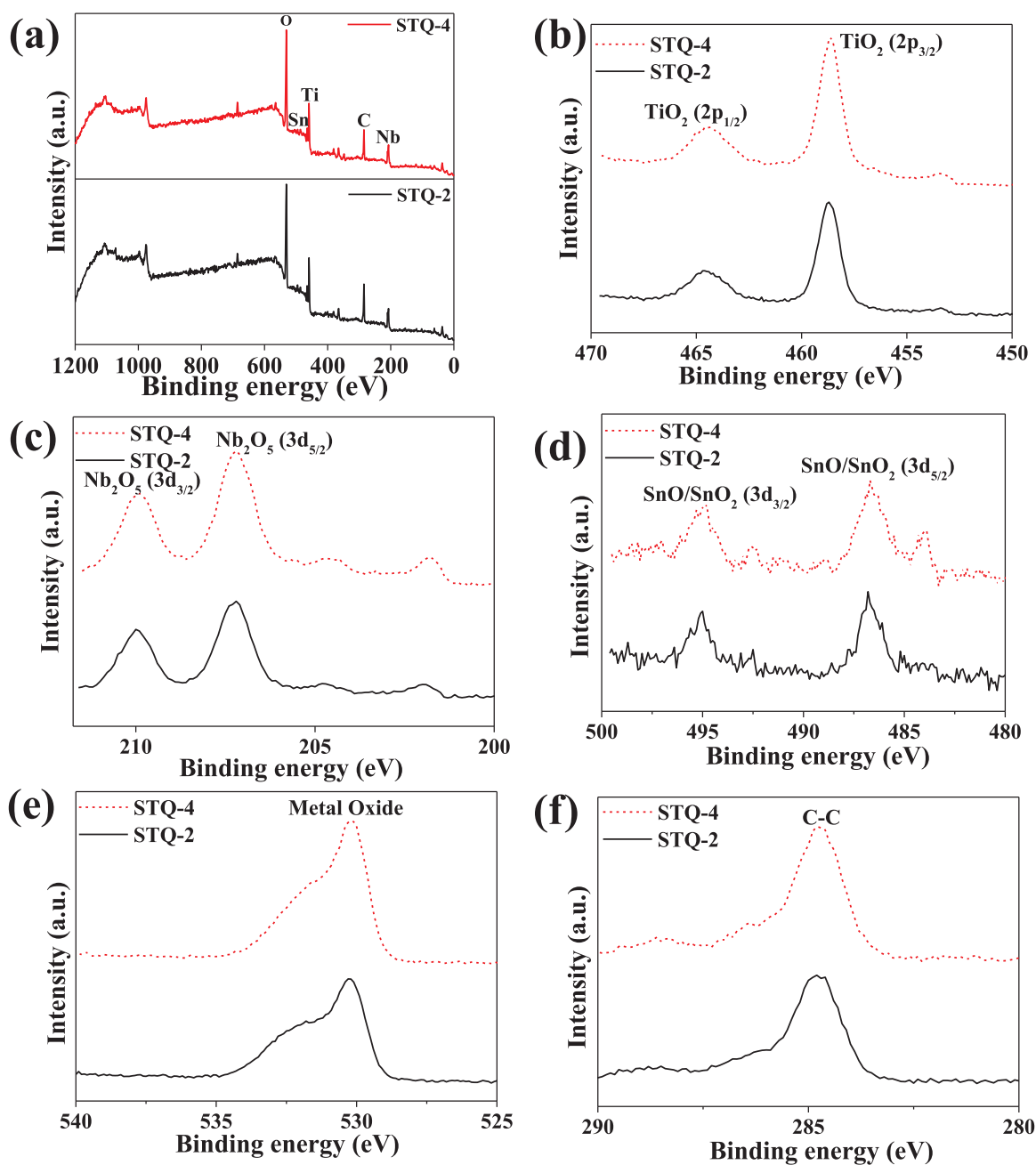


Fig. 7. (a) Wide XPS spectra of STQ-2 and STQ-4. High resolution XPS spectra of (b) Ti, (c) Nb, (d) Sn, (e) O and (f) C.

### 3.3. Composition of the oxide layer and electrochemical behavior of TNS alloys

The effect of alloy composition on the composition of the passive layer formed on the TNS alloys was evaluated by XPS. For this purpose, only STQ microstructures were evaluated. Fig. 7 shows the wide spectra of STQ-2 and STQ-4 alloy. The peaks associated with Ti, Nb and Sn are identified. The high resolution XPS spectra of Ti, Nb, Sn, O and C are also shown in Fig. 7 which, reveal that the surface oxide primarily consists of  $\text{TiO}_2$ ,  $\text{Nb}_2\text{O}_5$ , and  $\text{SnO/SnO}_2$ . The oxygen is present in form of metal oxides and hydroxides. The carbon peak observed is the adventitious carbon contamination from the atmosphere. Table 2 quantifies the concentration of elements in the passive layer. The composition of the passive layer formed on the STQ-2 and STQ-4 specimens is similar. Nevertheless, the fraction of Sn in the oxide layer is higher in STQ-4 as compared to STQ-2 in line with higher Sn content in the base

Table 2  
Quantification of the elements present in the passive oxide layer in at%.

Element	STQ-2 (at%)	STQ-4 (at%)
C	39.8	37.9
O	48.1	47.8
Ti	7.6	9.9
Nb	4.1	3.9
Sn	0.3	0.5

metal.

Fig. 8a shows Tafel plots of the STQ and A500 specimens. Both the TNS-2 and TNS-4 alloys show passivation behavior of Ti independent of the microstructure. The values of corrosion current density  $I_{\text{CORR}}$  and corrosion potential  $E_{\text{CORR}}$  as calculated by Tafel extrapolation method are compiled in Table 3. The corrosion rates of the STQ specimens are

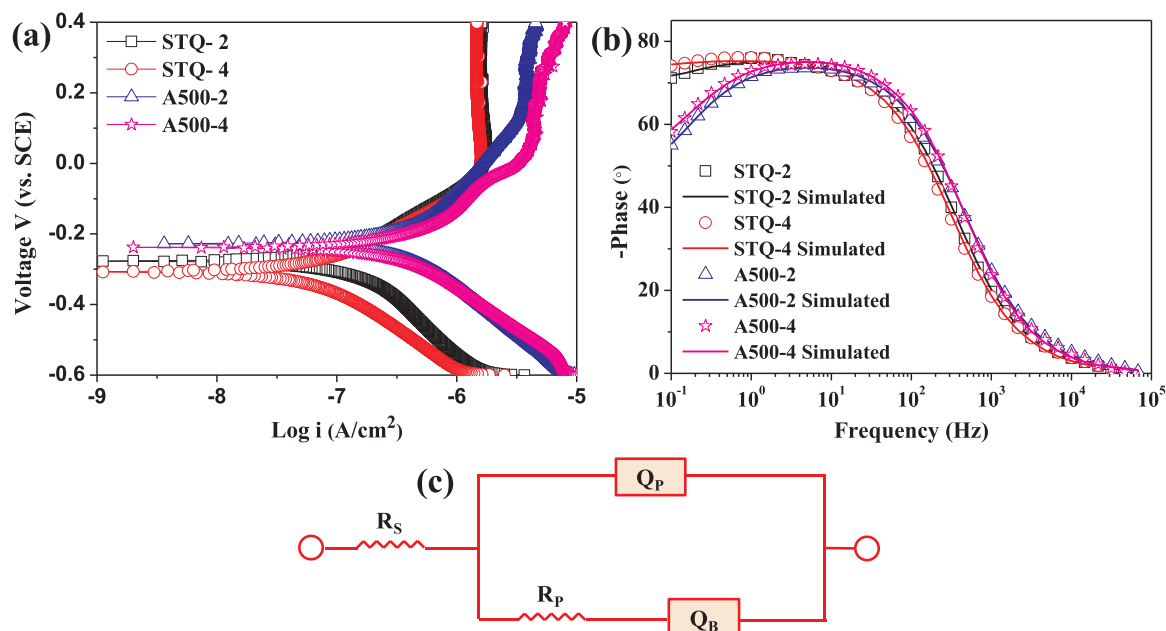


Fig. 8. (a) Tafel plot and (b) Bode-phase plot of STQ-(2, 4) and A500-(2, 4). (c) Equivalent circuit used to fit the impedance data.

lower than corresponding A500 specimens for both TNS-2 and TNS-4 alloys. The corrosion rate of STQ-4 is marginally lower than STQ-2. Similarly, the corrosion rate of A500-4 is slightly lower than A500-2. It suggests that the corrosion resistance of TNS-4 alloy is slightly better than TNS-2 alloys. Fig. 8b shows the Bode diagram (phase vs. frequency) of the STQ and A500 specimens. The experimentally measured spectra were modeled using the equivalent circuit (EQ) shown in Fig. 8c. The term  $R_s$  is the solution resistance. The circuit represents a bi-oxide layer model. The passive layer is composed of a porous outermost oxide layer and a compact inner oxide layer. The porous oxide layer is described by a resistance  $R_p$  and a constant phase element  $Q_p$ . The constant phase element represents a non-ideal capacitor and is described by a parameter 'n'. A value of  $n < 1$  represents a non-ideal capacitor. The inner compact oxide is described only by constant phase element  $Q_b$ . The values of the circuit elements are compiled in Table 3. The difference between the various specimens is in the values of  $Q_b$  which corresponds to the inner compact layer. The value is lower for STQ specimens as compared to A500 specimens indicating the superior nature of oxide layer formed on the former. The values of  $Q_b$  are lower for STQ-4 compared to STQ-2 and lower for A500-4 compared to A500-2. The values of  $Q_b$  corroborate the results of Tafel extrapolation that TNS-4 alloys have slightly better corrosion resistance than TNS-2 alloys.

The values of corrosion rates of the TNS alloys measured in this investigation are very low in both the single phase and aged microstructures. These corrosion rate values are similar to the corrosion rate of commercially pure titanium measured in SBF, which is a well studied biomaterial (Bahl et al., 2017a). The higher Sn content marginally improved the corrosion resistance in TNS alloys. A similar decrease in

corrosion rate of Ti-Nb-Sn with an increase in Sn content in NaCl solution has been reported previously (Zheng et al., 2006). In another investigation, increase in Sn content up to 6 wt% increased the corrosion resistance in Ti-Nb-Sn alloys due to the continuous suppression of  $\omega$  and  $\alpha''$  phases (Moraes et al., 2014). However, once the  $\beta$  phase was retained, a further increase in the Sn content led to a decrease in the corrosion resistance. The change in corrosion behavior with Sn content is not due to change in the phases present as only single  $\beta$  was present in both STQ-2 and STQ-4 alloys. Thus, the superior quality of oxide layer formed on TNS-4 alloy compared to TNS-2 revealed by impedance spectroscopy is responsible for better corrosion resistance in the former. The corrosion rates in the aged specimens are higher compared to their corresponding single  $\beta$  microstructures likely due to galvanic coupling between  $\beta$  and  $\alpha$  phases in the former, as reported previously (Bahl et al., 2017a). Overall, TNS alloys with up to 4 wt% Sn are suitable for biomedical applications from the point of view of electrochemical behavior.

### 3.4. Biological response of the TNS alloys

hMSCs are multipotent stem cells that can differentiate into osteoblasts. When implanted, an orthopedic device is likely to contact hMSCs. Thus, hMSCs cultured on these alloys are indicative of the biological response to these alloys. The DNA content of hMSCs as an indicator of cell attachment and proliferation is shown in Fig. 9. Both the alloys are cytocompatible as the hMSCs attached and proliferated with time. The Sn content up to 4 wt% did not affect the attachment and proliferation of hMSCs. The attachment and proliferation were also

Table 3  
Electrochemical parameters measured from Tafel plots and impedance spectroscopy.

Parameter	STQ-2	STQ-4	A500-2	A500-4
Corrosion current density $I_{CORR}$ ( $\times 10^{-7}$ A/cm <sup>2</sup> )	1.1 $\pm$ 0.6	0.7 $\pm$ 0.1	3.5 $\pm$ 0.5	2.7 $\pm$ 1.2
Corrosion potential $E_{CORR}$ (V vs. SCE)	-0.31 $\pm$ 0.03	-0.30 $\pm$ 0.02	-0.23 $\pm$ 0.04	-0.23 $\pm$ 0.03
Solution resistance $R_s$ ( $\Omega$ cm <sup>2</sup> )	26 $\pm$ 1	27 $\pm$ 7	30 $\pm$ 4	29 $\pm$ 5
Resistance $R_p$ ( $\times 10^5 \Omega$ cm <sup>2</sup> )	1.5 $\pm$ 0.8	0.7 $\pm$ 0.1	0.8 $\pm$ 0.2	1.6 $\pm$ 1.4
Constant phase element $Q_p$ ( $\times 10^{-5}$ F cm <sup>-2</sup> )	5.1 $\pm$ 0.6	4.9 $\pm$ 1.2	3.3 $\pm$ 0.2	3.6 $\pm$ 0.4
$n_p$	0.79 $\pm$ 0.08	0.84 $\pm$ 0.01	0.85 $\pm$ 0.02	0.88 $\pm$ 0.03
Constant phase element $Q_b$ ( $\times 10^{-6}$ F cm <sup>-2</sup> )	27.1 $\pm$ 17.3	1.4 $\pm$ 0.4	55.3 $\pm$ 31.2	35.1 $\pm$ 24.8
$n_b$	0.98 $\pm$ 0.01	0.94 $\pm$ 0.07	0.91 $\pm$ 0.08	0.85 $\pm$ 0.20

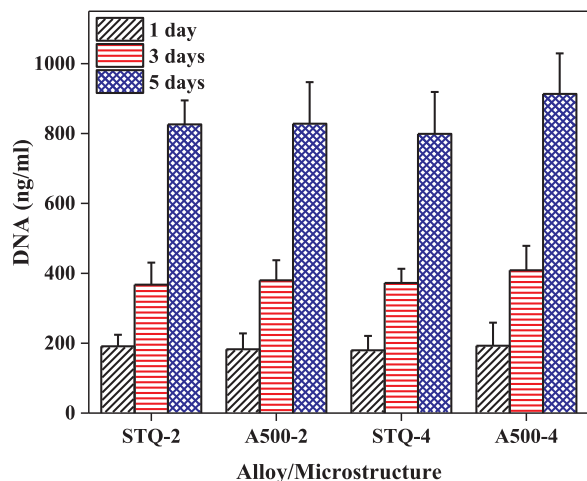


Fig. 9. DNA content on the specimens at 1 day, 3 days and 5 days after seeding cells.

found to be independent of the microstructure. The fluorescence micrographs of hMSCs at 1 day, 3 days and 5 days are shown in Fig. 10. The cells appear well spread at 1 day on all the specimens. The cell numbers increased with time and no difference in cell numbers was observed among the specimens as shown by DNA quantification (Fig. 9).

Osteogenic differentiation is characterized by increased expression of ALP, an early marker and deposition of minerals, which is taken as a late marker. The mineralization and ALP activity measured at 14 days to evaluate osteogenic differentiation is shown in Fig. 11. The mineral content and ALP activity were normalized to DNA content at 14 days. The two alloys TNS-2 and TNS-4 did not show any significant difference in the mineral deposited irrespective of the microstructure (Fig. 11a). The difference in ALP activity was not statistically significant on STQ-2 and STQ-4. Similarly, the ALP activity was not significantly different for A500-2 and A500-4. The ALP activity of A500-4 was statistically lower compared to STQ-2 and STQ-4. The ALP activity of A500-2 was

statistically lower compared to STQ-2. These results indicate that the Sn content up to 4 wt% does not markedly alter the osteogenic differentiation of hMSCs in TNS alloys. Although there is some statistically significant difference between the ALP activity of STQ and A500, the absolute difference is marginal. It can, therefore, be said that the dual phase microstructure does not significantly alter the osteogenic differentiation. Moreover, the mineral deposited as measured by ARS (Fig. 11a) was similar in the dual phase and single phase microstructures. The results of the cell studies presented here suggest that the TNS alloys with Sn content up to 4 wt% are suitable for biomedical application. In our previous work (Bahl et al., 2017a), it was found that Ti-32Nb-2Sn is cytocompatible and supports osteogenesis equally good as cp-Ti. Therefore, by comparing the results of this work with the previous report (Bahl et al., 2017a) it can be said that Ti-Nb-Sn alloys with up to 4 wt% Sn are equally cytocompatible as cp-Ti.

#### 4. Conclusion

In this investigation, two specially designed Sn containing  $\beta$  Ti alloys have been evaluated for their suitability for orthopedic implants. The effects of Sn content on desirable mechanical, electrochemical and biological properties have been evaluated. The role of Sn has been established in stabilizing a single  $\beta$  phase which essentially rendered the alloy suitable for implant applications. The elastic modulus reduced with an increase in Sn content in the single phase microstructure. The addition of higher Sn content increased the aspect ratio of  $\alpha$  precipitates on aging, rendering an overall increase in the strength of the alloy. The corrosion rates of alloys in single phase and dual phase (aged) microstructures were very low and thus suitable for implant applications. The corrosion resistance was higher for alloys with higher Sn content due to the superior nature of the oxide layer. The addition of Sn up to 4 wt% did not induce any cytotoxic effects on human mesenchymal stem cells indicating its biocompatible nature. The Sn containing alloys were found to be cytocompatible as they supported attachment, proliferation and more importantly osteogenic differentiation of stem cells. Overall, it can be said that the thermo-mechanically processed Sn containing  $\beta$  Ti alloys have the desired properties for orthopedic applications such as

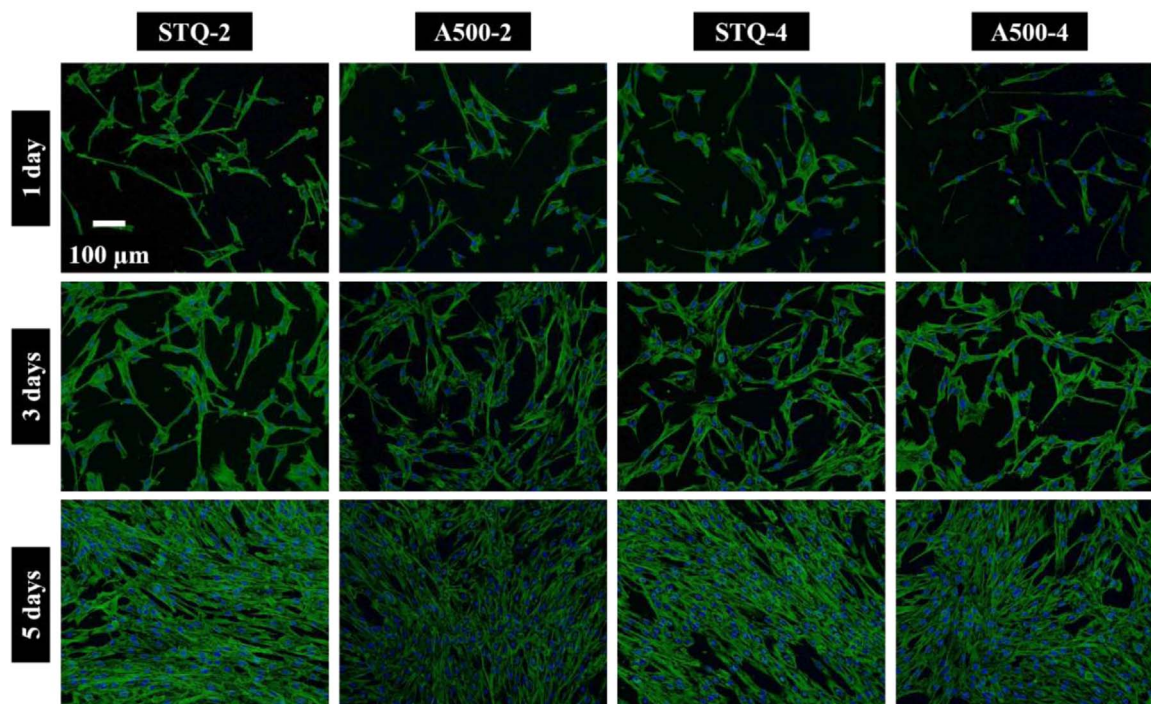


Fig. 10. Fluorescence micrographs of hMSCs at 1 day, 3 days and 5 days after seeding cells. The nuclei are shown in blue and the actin filaments are shown in green. (For interpretation of the references to color in this figure legend, the reader is referred to the web version of this article).

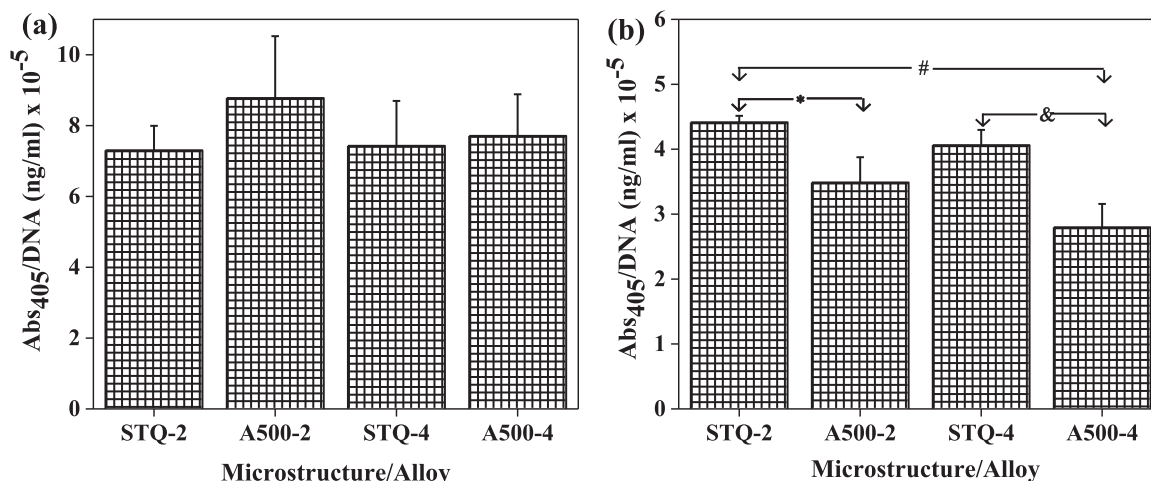


Fig. 11. Cell number normalized values of (a) Mineral deposition quantified by ARS and (b) ALP activity at 14 days. \*, # and & shows statistically significant differences at  $p < 0.05$ .

high strength, low elastic modulus, high corrosion resistance and excellent biocompatibility.

### Acknowledgements

The authors thankfully acknowledge Dr. Amit Bhattacharjee from Defence Metallurgical Research Laboratory, Hyderabad, India for his help. The authors acknowledge Department of Science and Technology (DST), India for the funding.

### References

- Abdel-Hady, M., Fuwa, H., Hinoshita, K., Kimura, H., Shinzato, Y., Morinaga, M., 2007. Phase stability change with Zr content in  $\beta$ -type Ti-Nb alloys. *Scr. Mater.* 57, 1000–1003.
- Bahl, S., Devadiga, A., Chatterjee, K., Suwas, S., Phase Stability Study of Recently Developed Metastable p-Ti ALLOY Ti-32Nb-2Sn for Orthopedic Applications, in: *Proceedings of the 13th World Conference on Titanium*. Wiley Online Library, 2016, pp. 935–938.
- Bahl, S., Krishnamurthy, A.S., Suwas, S., Chatterjee, K., 2017a. Controlled nanoscale precipitation to enhance the mechanical and biological performances of a metastable  $\beta$  Ti-Nb-Sn alloy for orthopedic applications. *Mater. Des.* 126, 226–237.
- Bahl, S., Shreyas, P., Trishul, M., Suwas, S., Chatterjee, K., 2015. Enhancing the mechanical and biological performance of a metallic biomaterial for orthopedic applications through changes in the surface oxide layer by nanocrystalline surface modification. *Nanoscale* 7, 7704–7716.
- Bahl, S., Suwas, S., Chatterjee, K., 2014. The importance of crystallographic texture in the use of titanium as an orthopedic biomaterial. *RSC Adv.* 4, 38078–38087.
- Bahl, S., Suwas, S., Ungar, T., Chatterjee, K., 2017b. Elucidating microstructural evolution and strengthening mechanisms in nanocrystalline surface induced by surface mechanical attrition treatment of stainless steel. *Acta Mater.* 122, 138–151.
- Banerjee, D., Williams, J., 2013. Perspectives on titanium science and technology. *Acta Mater.* 61, 844–879.
- Cardoso, F.F., Ferrandini, P.L., Lopes, E.S., Cremasco, A., Caram, R., 2014. Ti-Mo alloys employed as biomaterials: effects of composition and aging heat treatment on microstructure and mechanical behavior. *J. Mech. Behav. Biomed. Mater.* 32, 31–38.
- Dalmau, A., Pina, V.G., Devesa, F., Amigó, V., Muñoz, A.I., 2015. Electrochemical behavior of near-beta titanium biomedical alloys in phosphate buffer saline solution. *Mater. Sci. Eng. C* 48, 55–62.
- Griza, S., de Souza Sá, D.H.G., Batista, W.W., de Blas, J.C.G., Pereira, L.C., 2014. Microstructure and mechanical properties of hot rolled TiNbSn alloys. *Mater. Des.* 56, 200–208.
- Gurao, N., Manivasagam, G., Govindaraj, P., Asokamani, R., Suwas, S., 2013. Effect of texture and grain size on bio-corrosion response of ultrafine-grained titanium. *Metall. Mater. Trans. A* 44, 5602–5610.
- Hanada, S., Matsumoto, H., Watanabe, S., 2005. *Mechanical Compatibility of Titanium Implants in Hard Tissues*, International Congress Series. Elsevier, pp. 239–247.
- Hao, Y., Li, S., Sun, S., Yang, R., 2006. Effect of Zr and Sn on Young's modulus and superelasticity of Ti-Nb-based alloys. *Mater. Sci. Eng. A* 441, 112–118.
- Hao, Y., Li, S., Sun, S., Zheng, C., Yang, R., 2007. Elastic deformation behaviour of Ti-24Nb-4Zr-7.9 Sn for biomedical applications. *Acta Biomater.* 3, 277–286.
- Hsu, H.-C., Wu, S.-C., Hsu, S.-K., Syu, J.-Y., Ho, W.-F., 2013. The structure and mechanical properties of as-cast Ti-25Nb-xSn alloys for biomedical applications. *Mater. Sci. Eng. A* 568, 1–7.
- Li, S., Jia, M., Prima, F., Hao, Y., Yang, R., 2011. Improvements in nonlinear elasticity and strength by grain refinement in a titanium alloy with high oxygen content. *Scr. Mater.*

- 64, 1015–1018.
- Málek, J., Hnilica, F., Veselý, J., Smola, B., Kolařík, K., Fojt, J., Vlach, M., Kodetová, V., 2016. The effect of Zr on the microstructure and properties of Ti-35Nb-XZr alloy. *Mater. Sci. Eng. A* 675, 1–10.
- Matsumoto, H., Watanabe, S., Hanada, S., 2005. Beta TiNbSn alloys with low Young's modulus and high strength. *Mater. Trans.* 46, 1070–1078.
- Matsumoto, H., Watanabe, S., Hanada, S., 2007. Microstructures and mechanical properties of metastable  $\beta$  TiNbSn alloys cold rolled and heat treated. *J. Alloy. Compd.* 439, 146–155.
- Mencièrre, M.-L., Amouyel, T., Taviaux, J., Bayle, M., Laterza, C., Mertl, P., 2014. Fracture of the cobalt-chromium modular femoral neck component in total hip arthroplasty. *Orthop. Traumatol.: Surg. Res.* 100, 565–568.
- Miura, K., Yamada, N., Hanada, S., Jung, T.-K., Itoi, E., 2011. The bone tissue compatibility of a new Ti-Nb-Sn alloy with a low Young's modulus. *Acta Biomater.* 7, 2320–2326.
- Mohammed, M.T., Khan, Z.A., Geetha, M., Siddiquee, A.N., 2015. Microstructure, mechanical properties and electrochemical behavior of a novel biomedical titanium alloy subjected to thermo-mechanical processing including aging. *J. Alloy. Compd.* 634, 272–280.
- Moraes, P.E., Contieri, R.J., Lopes, E.S., Robin, A., Caram, R., 2014. Effects of Sn addition on the microstructure, mechanical properties and corrosion behavior of Ti-Nb-Sn alloys. *Mater. Charact.* 96, 273–281.
- Nie, J., 2003. Effects of precipitate shape and orientation on dispersion strengthening in magnesium alloys. *Scr. Mater.* 48, 1009–1015.
- Nie, J.F., Muddle, B.C., Polmear, I.J., 1996. The effect of precipitate shape and orientation on dispersion strengthening in high strength aluminium alloys. *Mater. Sci. Forum Trans. Tech. Publ.* 1257–1262.
- Niinomi, M., Nakai, M., Hieda, J., 2012. Development of new metallic alloys for biomedical applications. *Acta Biomater.* 8, 3888–3903.
- Norman, P., Iyengar, S., Svensson, I., Flivik, G., 2014. Fatigue fracture in dual modular revision total hip arthroplasty stems: failure analysis and computed tomography diagnostics in two cases. *J. Arthroplast.* 29, 850–855.
- Rosalbino, F., Maccio, D., Scavino, G., Saccone, A., 2012. In vitro corrosion behaviour of Ti-Nb-Sn shape memory alloys in Ringer's physiological solution. *J. Mater. Sci.: Mater. Med.* 23, 865–871.
- Salvador, C.A., Lopes, E.S., Ospina, C.A., Caram, R., 2016. Orthorhombic martensite formation upon aging in a Ti-30Nb-4Sn alloy. *Mater. Chem. Phys.* 183, 238–246.
- Suresh, K., Geetha, M., Richard, C., Landoulsi, J., Ramasawmy, H., Suwas, S., Asokamani, R., 2012. Effect of equal channel angular extrusion on wear and corrosion behavior of the orthopedic Ti-13Nb-13Zr alloy in simulated body fluid. *Mater. Sci. Eng. C* 32, 763–771.
- Suresh, K., Gurao, N., Singh, S., Suwas, S., Chattopadhyay, K., Zherebtsov, S., Salishchev, G., 2013. Effect of equal channel angular pressing on grain refinement and texture evolution in a biomedical alloy Ti 13Nb 13Zr. *Mater. Charact.* 82, 73–85.
- Wang, H., Hao, Y., He, S., Du, K., Li, T., Obbard, E., Hudspeth, J., Wang, J., Wang, Y., Wang, Y., 2017. Tracing the coupled atomic shear and shuffle for a cubic to a hexagonal crystal transition. *Scr. Mater.* 133, 70–74.
- Wang, X., Chen, Y., Xu, L., Liu, Z., Woo, K.-D., 2013. Effects of Sn content on the microstructure, mechanical properties and biocompatibility of Ti-Nb-Sn/hydroxyapatite biocomposites synthesized by powder metallurgy. *Mater. Des.* 49, 511–519.
- Yoshitani, J., Nakamura, T., Maruhashi, Y., Sasagawa, T., Ueshima, K., Funaki, K., 2016. Modular stem fracture at stem-sleeve junction after primary total hip arthroplasty. *J. Orthop. Sci.*
- Zhang, D., Mao, Y., Li, Y., Li, J., Yuan, M., Lin, J., 2013. Effect of ternary alloying elements on microstructure and superelasticity of Ti-Nb alloys. *Mater. Sci. Eng. A* 559, 706–710.
- Zheng, Y., Wang, B., Wang, J., Li, C., Zhao, L., 2006. Corrosion behaviour of Ti-Nb-Sn shape memory alloys in different simulated body solutions. *Mater. Sci. Eng. A* 438, 891–895.